VICTORIA UNIVERSITY

MELBOURNE AUSTRALIA

Assessment of cerebrovascular responses to physiological stimuli in identical twins using multimodal imaging and computational fluid dynamics

This is the Published version of the following publication

INNOVATIVE METHODOLOGY

Assessment of cerebrovascular responses to physiological stimuli in identical twins using multimodal imaging and computational fluid dynamics

Hannah J. Thomas,[1] Usaid Rana,[2,3,4] Channa E. Marsh,[1] Harrison T. Caddy,[2,3,4] Lachlan J. Kelsey,[2,3,4] Kurt J. Smith,[1,5,6] Daniel J. Green,[1]* and Barry J. Doyle[2,3,4,7,8]*

[1]*School of Human Sciences, The University of Western Australia, Perth, Australia;* [2]*Vascular Engineering Laboratory, Harry Perkins Institute of Medical Research, Queen Elizabeth II Medical Centre, Nedlands, Australia;* [3]*Centre for Medical Research, The University of Western Australia, Perth, Australia;* [4]*School of Engineering, The University of Western Australia, Perth, Australia;* [5]*Vascular Research Laboratory, School of Kinesiology, Lakehead University, Ontario, Canada;* [6]*Integrative Physiology Laboratory, Department of Kinesiology and Nutrition, University of Illinois, Chicago, Illinois;* [7]*Australian Research Council Centre for Personalised Therapeutics Technologies, Melbourne, Australia;* and [8]*British Heart Foundation Centre for Cardiovascular Science, The University of Edinburgh, Edinburgh, United Kingdom*

Thomas HJ, Rana U, Marsh CE, Caddy HT, Kelsey LJ, Smith KJ, Green DJ, Doyle BJ. Assessment of cerebrovascular responses to physiological stimuli in identical twins using multimodal imaging and computational fluid dynamics. *J Appl Physiol* 129: 1024–1032, 2020. First published September 3, 2020; doi:10.1152/japplphysiol. 00348.2020.—There is acknowledged variability in the Circle of Willis (CoW) in the general population, yet the structure and function relationship of the cerebrovasculature is poorly understood. We aimed to demonstrate the feasibility of combining high-resolution imaging techniques and computational fluid dynamics (CFD) to describe cerebrovascular structure and function in vivo. We tested our methodology by examining the null hypothesis that monozygotic twins (18–30 yr) would exhibit similar CoW structure and function. Six twin pairs underwent 3T magnetic resonance angiography of the head and neck and B-mode Doppler ultrasound for velocity and diameter recordings in the vertebral and internal carotid arteries under three conditions (rest, hypercapnia, and exercise). Artery diameter, length, tortuosity, and bifurcation angle were assessed in regions of interest of the CoW. We simulated hemodynamics to determine the cardiac-cycle time-averaged wall shear stress (TAWSS), oscillatory shear index (OSI), and relative residence time (RRT). We observed low and insignificant intraclass correlations (ICC) between twins in all regions for diameter (ICC range 0.000–0.657, $P > 0.05$), two of four regions for length (ICC range 0.355–0.368, $P > 0.05$), all regions for tortuosity (ICC range 0.270–0.505, $P > 0.05$), and all bifurcation angles (ICC range 0.000–0.547, $P > 0.05$). Similarly, no significant correlations were apparent for cerebral blood flow or CFD-derived measures of TAWSS, OSI, and RRT, at rest or in response to hypercapnia or exercise. Therefore, differences exist in CoW structure and associated shear stress in response to physiological stimulation. These data suggest that the structure, function, and health of cerebrovascular arteries are not primarily genetically dependent.

NEW & NOTEWORTHY There is acknowledged variability in the Circle of Willis in the general population, yet the structure and function relationship of the cerebrovasculature is poorly understood. Using a combination of magnetic resonance imaging, high-resolution Doppler ultrasound, and computational fluid dynamic modeling, we show that monozygotic twins exhibit differences in cerebrovascular structure and function when exposed to physiological stimuli. These data suggest that the morphology, function, and health of cerebrovascular arteries are not primarily genetically determined.

INTRODUCTION

Characterization of the structure and function of the cerebrovasculature is challenging, primarily due to the size and inaccessibility of the arterial anatomy within the bony skull. The development of imaging techniques such as computed tomography (CT), magnetic resonance imaging (MRI), and positron emission tomography (PET) have enabled characterization of anatomical structures, but, due to the relatively poor temporal resolution of these imaging modalities, the assessment of functional adaptation, that can occur very rapidly in response to changes in neuronal activation, blood gas concentrations, and blood pressure, remains problematic. The Circle of Willis (CoW) is of key importance in the maintenance of cerebral perfusion and, in turn, the ability to maintain healthy cerebral blood flow (CBF) in response to these rapidly occurring physiological changes. The CoW is, reputedly, highly variable between humans (5), yet there is some evidence to suggest the vascular structure is heritable (5). The structure and function of the CoW can be compared in monozygotic (MZ) twins to determine if the variability is influenced by genetics.

It has also become apparent that arterial shear stress is a key modulator of acute changes in artery function, health, and adaptation (7). Shear stress stimulates mechanoreceptors on the endothelial cell membrane that trigger signaling cascades to generate paracrine hormonal responses (6). Endothelium-derived substances such as nitric oxide, prostacyclin, and endothelium-derived hyperpolarizing factor play important roles in modulating artery function, remodeling, and atherosclerotic progression (8, 16). In peripheral and coronary arteries, episodic increases in shear stress induce upregulation of these antiatherogenic hormones and decrease cardiovascular events (7). However, the measurement of shear stress in cerebral arteries at rest and in response to physiological stimuli that
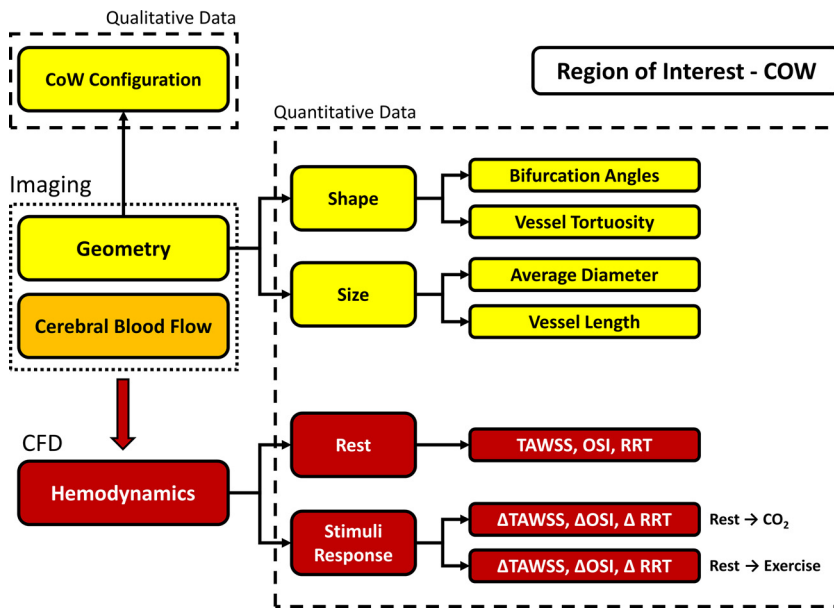

Fig. 1. Study plan. Participants were imaged using Doppler ultrasound (orange) and magnetic resonance angiography (yellow) to determine geometry and flow. These data were used to study the configuration of the Circle of Willis (CoW) and to investigate the hemodynamics under different conditions using computational fluid dynamics (CFD, red). TAWSS, time-averaged wall shear stress; OSI, oscillatory shear index; RRT, and relative residence time.

increase CBF (e.g., changes in blood pressure and CO_2) has not been reported in humans. Changes in shear stress in response to these common physiological stimuli may be influenced by variation in the anatomical structure of the CoW.

The aim of this study was to develop and describe a platform that enables characterization of the structure and function of the cerebrovasculature in humans. We aimed to combine duplex Doppler ultrasound and MRI to visualize the cerebrovascular anatomy and measure blood flow and hemodynamics. Using computational fluid dynamics (CFD), we aimed to calculate shear stress and flow-derived metrics to understand the link between structure and function. Finally, we aimed to study the behavior of these cerebral arteries under different environmental conditions (rest, hypercapnia, and exercise). To facilitate these aims, we posed the null hypothesis that the structure and function of the
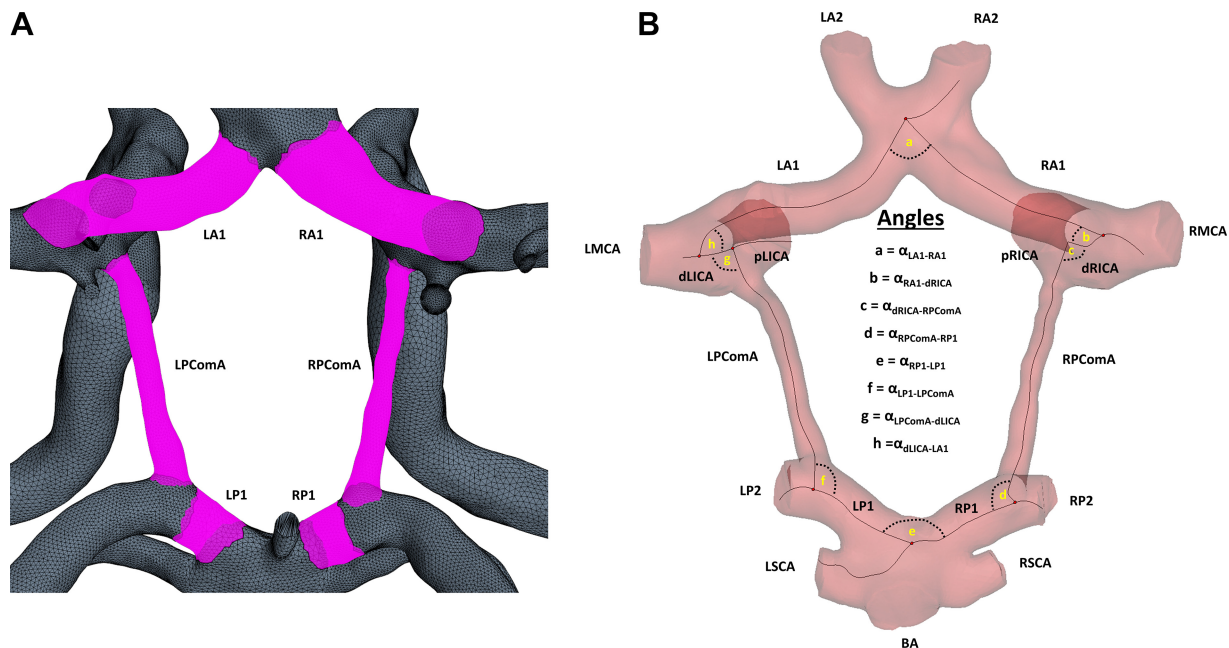

Fig. 2. A: regions of interest (highlighted magenta) for the Circle of Willis vessels from the global cerebrovasculature. B: centerlines and angles used in the geometric comparison. LA1, left anterior cerebral artery segment 1; LA2, left anterior cerebral artery segment 2; RA1, right anterior cerebral artery segment 1; RA2, right anterior cerebral artery segment 2; LMCA, left middle cerebral artery; PMCA, right middle cerebral artery; pLICA, proximal left internal carotid artery; pRICA, proximal right internal carotid artery; dLICA, distal left internal carotid artery; dRICA, distal right internal carotid artery; LPComA, left posterior communicating artery; RPComA, right posterior communicating artery; LP1, left posterior cerebral artery segment 1; LP2, left posterior cerebral artery segment 2; RP1, right posterior cerebral artery segment 1; RP2, right posterior cerebral artery segment 2; LSCA, left superior cerebellar artery; RSCA, right superior cerebellar artery; BA, basilar artery. αLA1-RA1 refers to the angle between LA1 and RA1, with similar notation used for the other angles. Note that we did not extract geometric (diameter, length, tortuosity) or hemodynamic data from LP1 or RP1 regions.

CoW, internal carotid (ICA), and vertebral arteries (VA) would not differ between MZ twins.

METHODS

Study Participants and Medical Imaging

The study was approved by The University of Western Australia (UWA) Human Research Ethics Committee and complied with the Declaration of Helsinki. We recruited six pairs of healthy MZ twins (three female and three male pairs) aged between 18 and 30 yr. A DNA cheek swab was obtained to confirm zygosity of twin pairs for inclusion in the study (EasyDNA AU, Springwood, QLD, Australia). Participants were informed of all experimental procedures and any potential associated risks, with written informed consent obtained before commencement of the study. Figure 1 illustrates the framework developed. We imaged the head and neck of each participant using 3T Time-of-Flight (3T TOF) magnetic resonance angiography (MRA; Siemens MAGNETOM Skyra) with a pixel size of 0.31 mm and slice thickness of 0.75 mm. We also used high-resolution Duplex ultrasound (DUS) to measure CBF in the ICAs and VAs. We measured velocity (Doppler ultrasound) and the intraluminal diameter (B-mode ultrasound) simultaneously using two identical 10-MHz multifrequency linear array probes and high-resolution ultrasound machines (Terason 3200). The reproducibility of DUS measurements of conduit arteries has a coefficient of variation of 6.7% (12). We used data captured over three consecutive cardiac cycles for each subject in this study. Further validation and process control steps for the DUS measurements can be found elsewhere (22). We measured CBF of each participant under three conditions: *1*) rest, after 5 min of seated rest; *2*) hypercapnia, after 5 min of breathing 6% CO_2 through a Douglas bag, and *3*) exercise, after 5 min of recumbent cycling at 90 watts.

MRA Image Processing, 3D Reconstruction and Analyses

Initially, we reduced the noise in the data using the discrete Gaussian and median filters in Mimics (v20, Materialise). Due to the high variability of pixel intensities throughout the cerebrovasculature, we used a region-growing algorithm by labeling pixels of similar intensity and connecting them to seed points (14). The inbuilt marching cubes algorithm in Mimics then generates 3D isosurfaces of the arterial segment. We smoothed the segmented geometry to within 5% reduction of original volume to remove artefacts from the reconstruction process. Finally, the outlets were cut perpendicular to the centerline at least two bifurcations away from the CoW to ensure that the geometry processing did not impact the CoW hemodynamics.

Structure was analyzed by qualitatively assessing the CoW configuration and quantitatively by assessing shape (vessel tortuosity and bifurcation angles) and size of the vessels (diameter and length). The CoW was divided into its six major vessels (Fig. 2*A*), and bifurcation angles were also measured throughout (Fig. 2*B*). We did not extract data from the left and right posterior cerebral artery segment of the CoW due to uncertainty; defining regions of interest of these vessels is challenging because of the complex bifurcating nature of the area (Fig. 2*A*). We paired data for twins together for comparative analyses.

Computational Fluid Dynamics

All CFD was performed in STAR-CCM+ (v11, Siemens).

Computational mesh. The inlet was extended (15) to ensure that flow is developed upon reaching the geometry. The outlets were extended by 11 times the outlet diameter. Polyhedral elements were used throughout the fluid core with 20 layers of prisms at the near wall boundary. The density of the mesh was set proportional to the local vessel radius to achieve accurate and efficient solution computation across varying vessel sizes. Mesh quality was thoroughly assessed and verified using the grid convergence index (GCI; see Refs. 2 and 21).
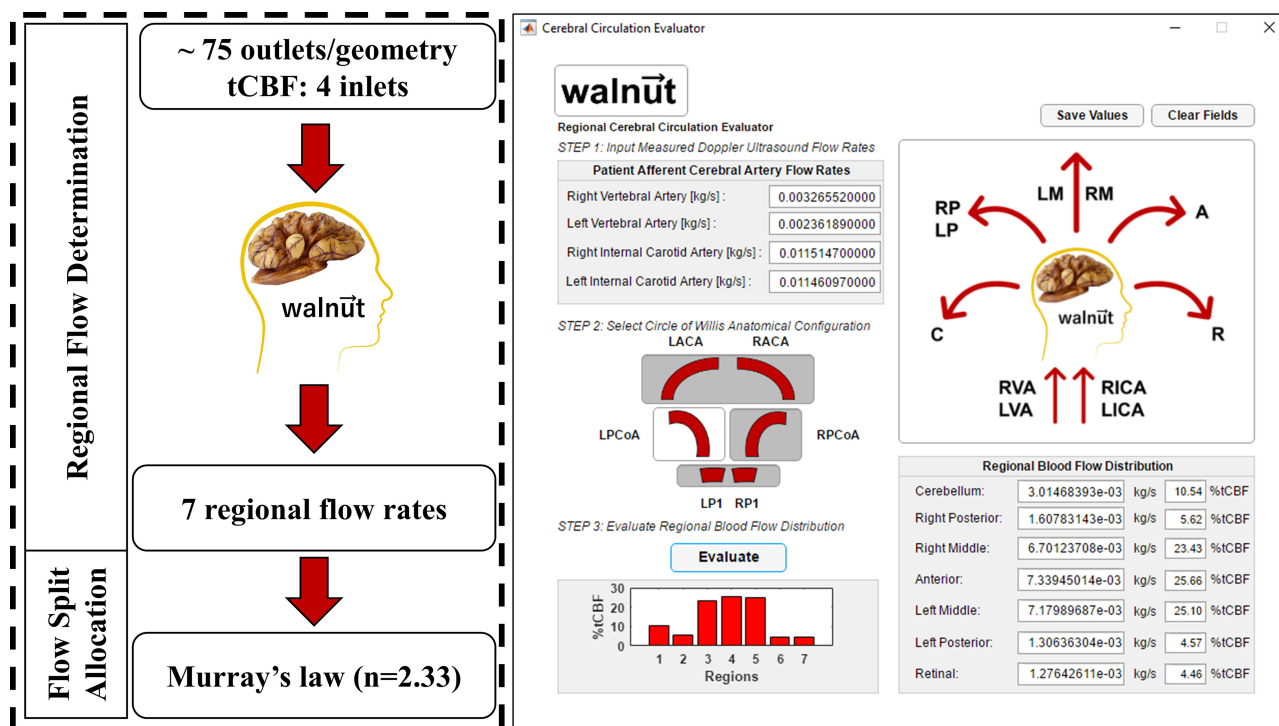

Fig. 3. *Left*, outlet condition assignment process; *right*, walnut application user interface. CBF, cerebral blood flow; LACA, left anterior cerebral artery; RACA, right anterior cerebral artery; LPCoA, left posterior communicating artery; RPCoA, right posterior communicating artery; LP1, left posterior cerebral artery segment 1; RP1, right posterior cerebral artery segment 1; RP, right posterior; LP, left posterior; RVA, right vertebral artery; LVA, left vertebral artery; RICA, right internal carotid artery; LICA, left internal carotid artery; LM, left middle; RM, right middle; A, anterior; R, retinal; C, cerebellum.

GCI was investigated using the subject that recorded the highest velocity DUS measurements, and data were deemed independent of mesh size when the GCI was <3%. Final meshes ranged from 11.2 to 19.5 million cells per geometry.

Inlet flow conditions. The DUS measurements of three cardiac cycles at the left and right ICAs and left and right VAs were processed and implemented as mass flow waveforms for each subject. The DUS was first fit with a spline containing 1,000 control points, before being smoothed and peak aligned. Data from the three cycles were then averaged into a single waveform for each vessel. Therefore, we had three inlet flow conditions (rest, hypercapnia, and exercise) for each subject, and these flow data were applied as plug profiles to the extended inlet. A detailed flowchart and example smoothing are provided in Supplemental Fig. S1 (all Supplemental data can be found at https://doi.org/10.5281/zenodo.3784208).

Outlet flow conditions. Outlet boundary conditions were specified as mass flow split ratios to mimic the CBF demand in the different regions of the brain. We chose to use flow splits instead of resistance-based models (1, 14, 19, 20, 24), since the geometries were complex (~75 outlets/geometry) and we did not have distal pressure or flow data. The assignment of outlet conditions was conducted in two steps: regional flow determination, followed by flow split allocation (Fig. 3). We developed a novel application called walnut in MATLAB (Mathworks) to streamline this process.

Within walnut, we determined the CBF received by each region of the brain by using the average inlet mass flows from 94 subject's regional CBFs (rCBFs) from a previous study (23). The algorithm accounts for the CoW configuration and subject-specific inlet flows, and then solves a linear system of equations to output rCBF. These regional flow rates were then used to determine the flow expected at each outlet within its region by implementing Murray's law with an exponent of 2.33 (3, 10). The code used for calculating the distribution of CBF (walnut) is provided in Supplemental Code S1.

Physical assumptions. We assumed the vessel walls were rigid with a no-slip condition, which has been used extensively in cerebral hemodynamics modeling (13, 14, 17–19). We calculated the Reynolds number (Re) at the inlet of each subject and found peak Re at rest to be ~400. The Re for the greatest velocity measured in any subject was during hypercapnia and only reached ~750. Therefore, we modeled each simulation using a laminar flow model. Blood was modeled as an incompressible fluid with constant density of 1050 kg/m^3 (4, 9, 14) and we used the Carreau-Yasuda viscosity model as it has shown good agreement with experimental data in the CoW (11).

Simulations and data. We solved the Navier-Stokes equations using the finite volume method in STAR-CCM+. Simulations were executed on Magnus, a Cray XC40 supercomputer (Pawsey Super-computing Centre, Perth, Australia) that houses 1,488 compute nodes, each collectively providing 24 cores/node. Each simulation was run across 25 nodes using 512 cores, requiring an average of 2,000 core hours to complete, equating to roughly 4 h of run time per simulation. We used an implicit unsteady segregated flow solver, the Semi-Implicit Method for Pressure Linked Equations (SIMPLE), to couple the pressure and velocity equations. First-order temporal discretization was used, since it was adequate to reach convergence. Automated time-step control was implemented (using an inbuilt solver) to attain a specified temporal resolution using the Courant number; time step was varied between 0.001 and 0.005 s. A new time step was triggered if absolute continuity or momentum residuals fell below a value of 10^{-9}. Once data had become independent of cardiac cycle, we calculated time-averaged wall shear stress (TAWSS), oscillatory shear index (OSI), and relative residence time (RRT) from the final cardiac
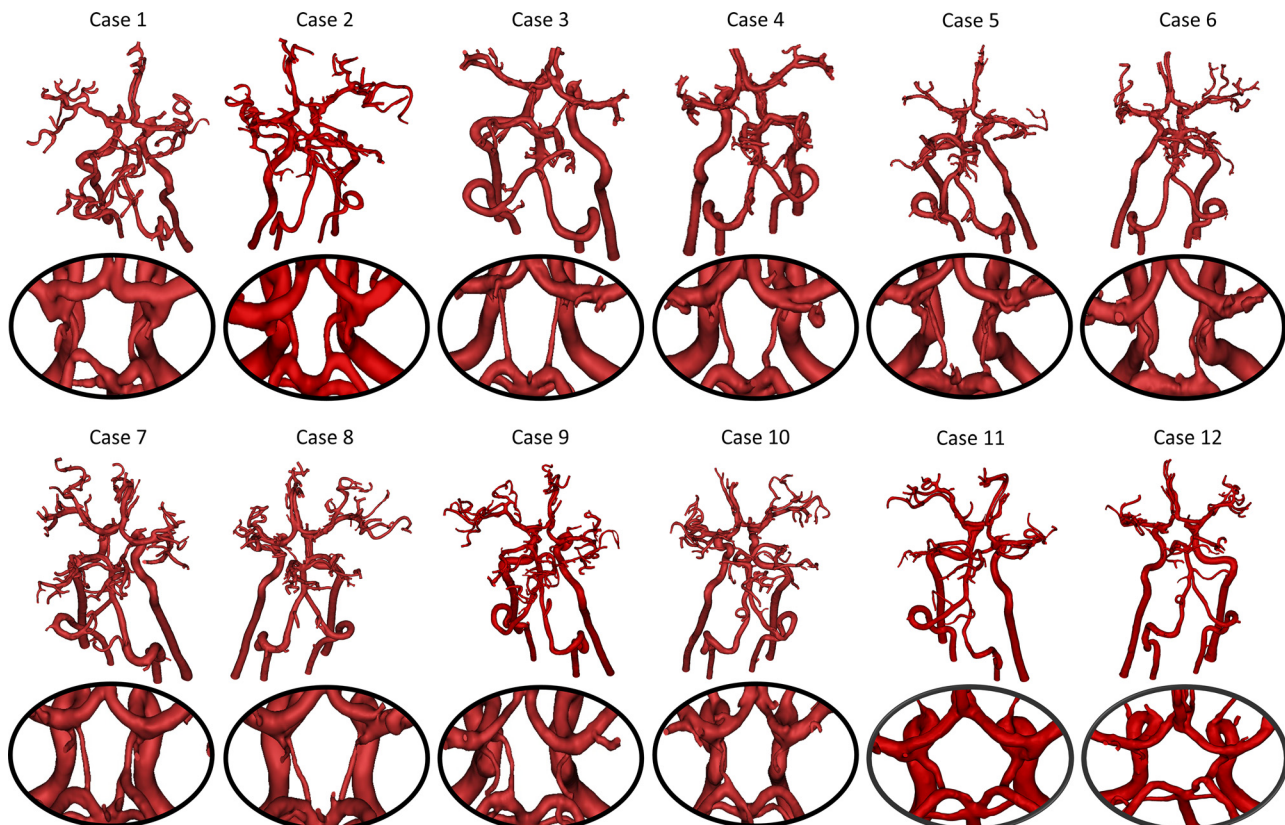

Fig. 4. 3D reconstructions for each case with their Circle of Willis (CoW) regions highlighted. *Cases 1–8* and *11* had complete CoWs, whereas *cases 9* and *10* had incomplete right posterior communicating artery and *case 12* had incomplete left posterior communicating artery.

cycle for each participant and compared data across the six major vessels of the CoW region.

Statistics. Statistical analyses were performed using STATA 11 software (StataCorp, College Station, TX). All data are reported as group means ± SD. Mixed-effects models were fitted, and then post-estimation intraclass correlations (ICC) were used to calculate correlations for MZ twin pairs. The subsequent ICC and their respective P-values and 95% confidence intervals (CIs) are presented in Tables 1–4. Statistical significance was assumed at $P < 0.05$.

RESULTS

MRI Measure of the Circle of Willis Configuration and Vessel Morphology at Rest

Participants were 24.8 ± 3.3 yr old with a BMI of 23.2 ± 5.5 kg/m^2. Using measurements from the MRA 3D reconstructions of the CoW from 3T time-of-flight (3T TOF) magnetic resonance angiography (MRA), we observed that nine participants had typical and complete CoW configurations, two (*cases 9* and *10*) had incomplete right posterior communicating arteries (RPComA), and one (*case 12*) had an incomplete left posterior communicating artery (LPComA) (Fig. 4).

Diameter. ICCs for vessel diameter indicate a poor to moderate correlation between twins in a pair, with insignificant associations (ICC ranging from 0.000 to 0.657, all $P > 0.05$; Table 1). Variation in vessel diameter between twins can be seen in Supplemental Table S1.

Length. ICCs for vessel length indicated a poor to moderate correlation between twins in a pair with two vessel regions,

with LA1 (ICC 0.805, 95% CI 0.407–0.961, $P < 0.01$) and LPComA (ICC 0.663, 95% CI 0.189–0.943, $P < 0.05$) showing significance while the other two regions were not significant (Table 1). Variation in vessel length between twins can be seen in Supplemental Table S1.

Tortuosity. ICCs for vessel tortuosity also indicated a poor correlation between twins in a pair (ICC ranging from 0.270 to 0.505, all $P > 0.05$; Table 1). Differences in vessel tortuosity across all regions of the CoW in twin pairs can be seen in Supplemental Table S1.

Bifurcation angle. ICCs of bifurcation angles indicated a poor correlation between twins in a pair, with no regions showing significant correlations (ICC ranging from 0.000 to 0.547, all $P > 0.05$; Table 1). There were differences in bifurcation angle across all regions of the CoW in twin pairs (Supplemental Table S2). We measured major differences between individuals with the maximum difference in bifurcation angle between the left and right posterior cerebral arteries (angle e) of ~50° in *cases 5* and *6*. In contrast, *cases 1* and *2* had four bifurcations with less than 5° difference. Therefore, differences in bifurcation angle between twins in a pair varied across twin pairs.

DUS Measures of Diameter and Cerebral Blood Flow at Rest and in Response to Stimulus

Diameter. Poor ICCs were seen in vessel diameter measured by DUS at rest (ICC ranging from 0.000 to 0.413, all $P > 0.05$), in change from rest to hypercapnia (ICC ranging from 0.000 to 0.095, all $P > 0.05$), and change from rest to exercise (ICC ranging from 0.000 to 0.331, all $P > 0.05$) (Table 2). Differences in vessel diameter in all twin pairs can be seen in Supplemental Table S3.

Cerebral blood flow. Poor ICCs were seen in CBF measured by DUS at rest (ICC ranging from 0.000 to 0.477, all $P > 0.05$), in change from rest to hypercapnia (ICC ranging from 0.000 to 0.312, all $P > 0.05$), and change from rest to exercise (ICC ranging from 0.000 to 0.554, all $P > 0.05$) (Table 2). Observed differences in CBF in all twin pairs can be seen in Supplemental Table S4.

CFD Measures of Function at Rest and in Response to Stimulus

CFD measures of function at rest. We found weak ICCs at rest in all regions in TAWSS (ICC ranging from 0.000 to 0.602, all $P > 0.05$), OSI (ICC ranging from 0.000 to 0.144, all $P > 0.05$), and RRT (ICC ranging from 0.000 to 0.559, all $P > 0.05$) between twins in a pair (Table 3). Resting differences between twins in TAWSS, OSI, and RRT are shown in Supplemental Table S5. Figure 5 depicts examples of qualitative hemodynamic data distributions for a twin pair under rest conditions (*cases 3* and *4*). Video examples of instantaneous wall shear stress and velocity over a cardiac cycle, for a single case, can be viewed in Supplemental Video S1. Because of the individual CoW geometries imaged with MRA and CBF measured with DUS, there was major variation in the hemodynamic calculations.

CFD measures of function in response to hypercapnia. ICCs for the change from rest to hypercapnia in TAWSS indicate a poor correlation between twins in a pair (ICC ranging from 0.000 to 596, all $P > 0.05$; Table 4). ICCs for the change from

Table 1. *Magnetic resonance imaging measures of structure in the CoW*

	Average ± SD	ICC	P Value	95% CI
Vessel diameter				
LA1	3.1 ± 0.5	0.000	1	0–0
RA1	2.9 ± 0.4	0.183	0.326	0.001–0.975
LPComA	1.6 ± 0.3	0.657	0.064	0.161–0.950
RPComA	1.9 ± 0.5	0.611	0.063	0.135–0.941
Vessel length				
LA1	11.4 ± 2.3	0.805	0.006*	0.407–0.961
RA1	9.8 ± 2.6	0.368	0.175	0.029–0.919
LPComA	11.3 ± 2.1	0.663	0.042*	0.189–0.943
RPComA	11.5 ± 2.4	0.355	0.206	0.019–0.940
Vessel tortuosity				
LA1	0.09 ± 0.02	0.270	0.250	0.008–0.941
RA1	0.08 ± 0.05	0.431	0.133	0.051–0.915
LPComA	0.12 ± 0.07	0.452	0.124	0.058–0.917
RPComA	0.12 ± 0.08	0.505	0.112	0.070–0.933
Bifurcation angle				
A	108.6 ± 23.1	0.245	0.271	0.006–0.950
B	95.2 ± 15.6	0.291	0.233	0.012–0.935
C	95.8 ± 18.8	0.460	0.138	0.050–0.932
D	93.8 ± 17.7	0.000	1	0–0
E	115.4 ± 24.0	0.547	0.072	0.112–0.921
F	101.7 ± 10.5	0.447	0.170	0.037–0.945
G	89.9 ± 9.4	0.228	0.315	0.002–0.978
H	92.8 ± 11.8	0.359	0.182	0.026–0.921

Shown are averages ± SD, intraclass correlation (ICC), *P* value, and confidence intervals of vessel length, diameter, tortuosity, and bifurcation angles at rest. Diameter, length, and tortuosity dimension data are in mm. Bifurcation angles are in degrees. Refer to Fig. 2 for locations of each vessel segment and angle. CoW, Circle of Willis; LA1, left anterior cerebral artery segment 1; RA1, right anterior cerebral artery segment 1; LPComA, left posterior communicating artery; RPComA, right posterior communicating artery. *$P < 0.05$.

Table 2. *Duplex ultrasound measures of function in the CoW*

	Average ± SD	ICC	*P* Value	95% CI
Diameter at rest				
RICA	0.470 ± 0.035	0.000	1	0–0
LICA	0.473 ± 0.042	0.000	1	0–0
RVA	0.358 ± 0.047	0.413	0.145	0.044–0.916
LVA	0.365 ± 0.058	0.000	1	0–0
ΔDiameter (rest to hypercapnia)				
RICA	0.023 ± 0.024	0.000	1	0–0
LICA	0.029 ± 0.021	0.059	0.443	0–1
RVA	0.012 ± 0.018	0.000	1	0–0
LVA	0.005 ± 0.041	0.095	0.407	0.000–0.999
ΔDiameter (rest to exercise)				
RICA	−0.001 ± 0.020	0.331	0.202	0.019–0.925
LICA	−0.030 ± 0.145	0.000	1	0–0
RVA	−0.034 ± 0.113	0.000	1	0–0
LVA	−0.006 ± 0.033	0.138	0.367	0.000–0.992
Cerebral blood flow at rest				
RICA	5.747 ± 2.858	0.477	0.106	0.071–0.916
LICA	7.922 ± 2.141	0.147	0.359	0.000–0.989
RVA	2.136 ± 0.729	0.000	1	0–0
LVA	3.169 ± 2.409	0.000	1	0–0
ΔFlow (rest to hypercapnia)				
RICA	5.162 ± 2.885	0.312	0.216	0.015–0.929
LICA	3.765 ± 2.875	0.184	0.325	0.001–0.975
RVA	1.093 ± 0.557	0.000	1	0–0
LVA	0.296 ± 2.322	0.000	1	0–0
ΔFlow (rest to exercise)				
RICA	2.836 ± 2.667	0.554	0.069	0.116–0.921
LICA	0.968 ± 3.378	0.000	1	0–0
RVA	0.199 ± 1.135	0.000	1	0–0
LVA	−0.223 ± 2.118	0.000	1	0–0

Shown are averages ± SD, intraclass correlation (ICC), *P* value, and confidence intervals of vessel diameter and cerebral blood flow at rest and change in response to stimulus (rest to hypercapnia and rest to exercise). Diameter data are in mm. Flow data are in ml/min. CoW, Circle of Willis; RICA, right internal carotid artery; LICA, left internal carotid artery; RVA, right vertebral artery; LVA, left vertebral artery.

rest to hypercapnia in both OSI and RRT were zero for all regions (all ICC 0.000, all $P > 0.05$; Table 4). The change in hemodynamics in TAWSS, OSI, and RRT due to hypercapnia are shown in Supplemental Table S6.

Table 3. *Computational fluid dynamic measures of function in the CoW*

	Average ± SD	ICC	*P* Value	95% CI
TAWSS				
LA1	5.344 ± 3.524	0.602	0.0503	0.152–0.927
RA1	2.718 ± 1.898	0.427	0.136	0.049–0.915
LPComA	5.880 ± 4.437	0.000	1	0–0
RPComA	3.523 ± 1.986	0.057	0.449	0–1
OSI				
LA1	0.039 ± 0.079	0.061	0.440	0–1
RA1	0.078 ± 0.082	0.000	1	0–0
LPComA	0.112 ± 0.079	0.144	0.376	0.000–0.995
RPComA	0.186 ± 0.078	0.000	1	0–0
RRT				
LA1	0.309 ± 0.189	0.559	0.067	0.120–0.922
RA1	0.794 ± 0.824	0.000	1	0–0
LPComA	0.441 ± 0.470	0.000	1	0–0
RPComA	0.742 ± 0.595	0.050	0.456	0–1

Shown are averages ± SD, intraclass correlation (ICC), *P* value, and confidence intervals of vessel time-averaged wall shear stress (TAWSS), oscillatory shear index (OSI), and relative residence time (RRT) at rest. For each region of the Circle of Willis (CoW) see Fig. 2*A*. Units for TAWWS are Pa, OSI is dimensionless, and RRT is 1/Pa. LA1, left anterior cerebral artery segment 1; RA1, right anterior cerebral artery segment 1; LPComA, left posterior communicating artery; RPComA, right posterior communicating artery.

CFD measures of function in response to exercise. ICCs for the change from rest to exercise in TAWSS indicate a poor correlation between twins in a pair, with just one region, LPComA (ICC 0.775, 95% CI 0.325–0.961, $P < 0.05$), showing significance while the other three regions were zero (all ICC 0.000, all $P > 0.05$) (Table 4). ICCs for the change from rest to exercise in both OSI and RRT were zero for all regions (all ICC 0.000, all $P > 0.05$; Table 4). The change in hemodynamics in TAWSS, OSI, and RRT due to exercise are shown in Supplemental Table S7.

DISCUSSION

This is the first study to examine cerebrovascular structure and function in MZ twins under different physiological conditions using combined medical imaging and CFD modeling. Our key findings are that we observed only poor to moderate ICCs between twins in geometric parameters relating to vessel length, diameter, tortuosity, and bifurcation angle. In addition, cerebrovascular functional indexes were not significantly correlated. There were differences between twins in a pair in terms of diameter and blood flow change, and large differences were apparent in intracranial CFD-derived measures of TAWSS, OSI, and the RRT of blood cells. These data suggest that the structure of the vascular tree differs between MZ twins and that even larger differences can exist in cerebrovascular function under conditions associated with typical commonplace physiological stress.
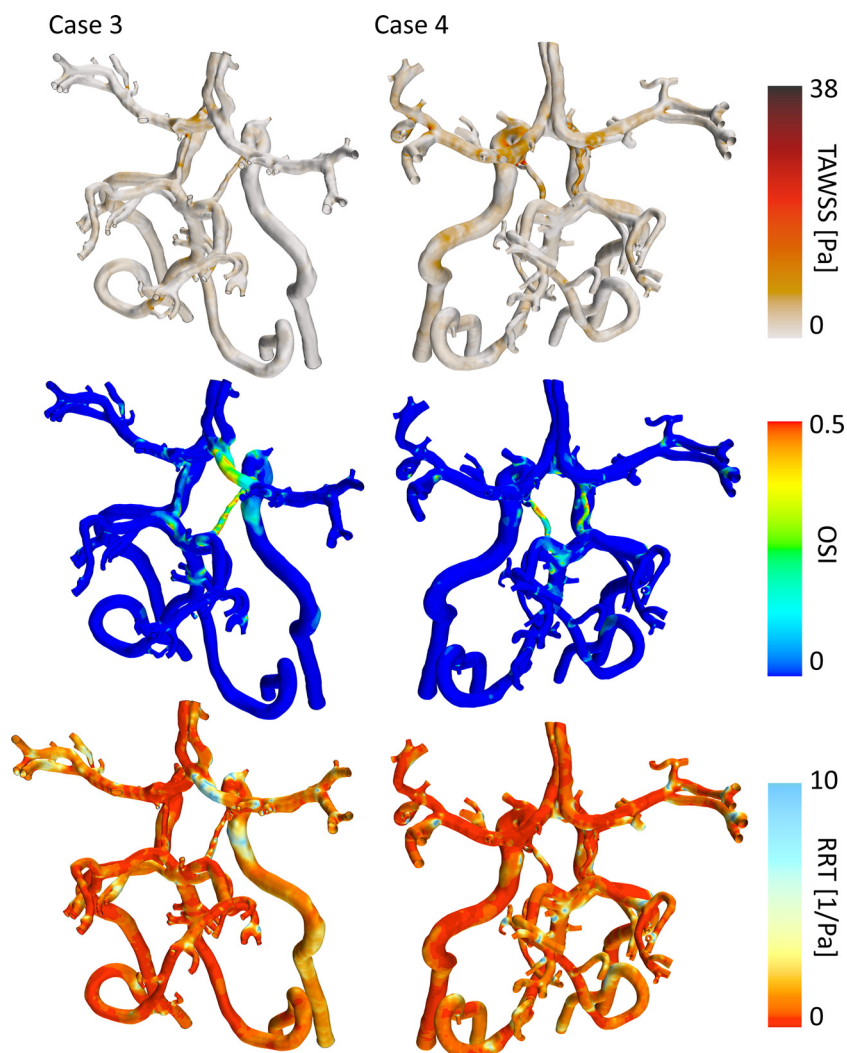
Fig. 5. Computational hemodynamic data at rest for *cases 3* and *4*. *Top*, time-averaged wall shear stress (TAWSS); *center*, oscillatory shear index (OSI); *bottom*, relative residence time (RRT). TAWSS is scaled to a peak of 38 Pa, which is a level known to be extreme.

We found marked differences in vessel diameter change, change in CBF, and change in TAWSS, OSI, and the RRT of blood particles. It is now well established that arterial shear stress is a key modulator of acute change in artery function, alongside chronic impacts on endothelial health and adaptation (7). One determinant of shear stress is the anatomical structure of the vessel bed, and interindividual differences in CoW geometry are typically very large (5). Our study indicates that subjects with matching DNA exhibit striking differences in anatomical determinants of shear, and even more substantial differences in TAWSS, OSI, and RRT between twins. These differences are being driven by changes in carotid and vertebral artery blood flow (due to differing CBF demands of the brain). Our data therefore indicate that, despite having similar genetics, CoW geometry and the function of the vessels differ even when exposed to standardized stimuli. These data highlight the importance of quantifying both the structure and function of cerebral arteries in humans.

Taken together, our data have some potential implications. Function and stress within the artery are influenced by environmental factors such as hypercapnia and exercise. Although our study was not planned or powered to identify the individual environmental factors that play the most important role in

influencing both structural and functional measures, future experiments in larger cohorts would be able to do so. Forgo and colleagues (5) assessed, using TOF MRA and transcranial Doppler sonography, whether heritability plays a role in the formation of the variants of the CoW or if they are influenced mostly by environmental factors. This study used both monozygotic and dizygotic twins and found that anatomical variants of the CoW, which are common and may predispose individuals to cerebrovascular events, are potentially shaped and influenced by environmental factors. Our study adds to this by using high-resolution Duplex ultrasound to determine CBF and calculating determinants of cerebrovascular function using CFD. The addition of functional measures expands on the conclusions of Forgo and colleagues that there seems to be little, if any, correlation between MZ twins, suggesting a low contribution of heritability to the structure and function of the cerebrovasculature.

A strength of this study is the use of both duplex Doppler ultrasound and MRI. The concurrent use of CFD has allowed us to highlight the importance of measuring both structure and function of the cerebrovasculature. Despite advances in imaging technology, significant spatial and temporal limitations

Table 4. *Computational fluid dynamic measures of function in the CoW*

	Average ± SD	ICC	P Value	95% CI
ΔTAWSS (rest to hypercapnia)				
LA1	2.202 ± 3.155	0.296	0.229	0.012–0.933
RA1	3.995 ± 4.282	0.483	0.103	0.074–0.916
LPComA	3.502 ± 5.833	0.000	1	0–0
RPComA	3.470 ± 4.972	0.596	0.069	0.124–0.939
ΔOSI (rest to hypercapnia)				
LA1	−0.006 ± 0.088	0.000	1	0–0
RA1	−0.036 ± 0.093	0.000	1	0–0
LPComA	0.000 ± 0.071	0.000	1	0–0
RPComA	−0.040 ± 0.070	0.000	1	0–0
ΔRRT (rest to hypercapnia)				
LA1	−0.089 ± 0.174	0.000	1	0–0
RA1	−0.521 ± 0.838	0.000	1	0–0
LPComA	−0.164 ± 0.495	0.000	1	0–0
RPComA	−0.373 ± 0.526	0.000	1	0–0
ΔTAWSS (rest to exercise)				
LA1	1.755 ± 2.945	0.000	1	0–0
RA1	1.972 ± 2.200	0.000	1	0–0
LPComA	5.713 ± 7.679	0.775	0.017*	0.325–0.961
RPComA	2.834 ± 3.368	0.000	1	0–0
ΔOSI (rest to exercise)				
LA1	0.007 ± 0.059	0.000	1	0–0
RA1	−0.034 ± 0.095	0.000	1	0–0
LPComA	0.058 ± 0.095	0.000	1	0–0
RPComA	−0.013 ± 0.110	0.000	1	0–0
ΔRRT (rest to exercise)				
LA1	−0.083 ± 0.161	0.000	1	0–0
RA1	−0.456 ± 0.883	0.000	1	0–0
LPComA	−0.097 ± 0.554	0.000	1	0–0
RPComA	−0.365 ± 0.427	0.000	1	0–0

Shown are averages ± SD, intraclass correlation (ICC), P value, and confidence intervals of change in vessel time-averaged wall shear stress (TAWSS), oscillatory shear index (OSI), and relative residence time (RRT) during stimulation (rest to hypercapnia and rest to exercise). For each region of the Circle of Willis (CoW) see Fig. 2*A*. Units for TAWWS, Pa, and OSI are dimensionless and RRT = 1/Pa. LA1, left anterior cerebral artery segment 1; RA1, right anterior cerebral artery segment 1; LPComA, left posterior communicating artery; RPComA, right posterior communicating artery. *$P < 0.05$.

remain when attempting to dynamically image the smaller vessels inside the bony skull. The use of contemporary MRI improves imaging resolution. We assessed one pair of individuals using both 1.5- and 3T magnets, with results indicating that the 3T approach results in substantially less variability and less partial rendering of arterialization. This has implications for the interpretation of previous studies that have relied on lower-resolution imaging or used a combination of magnet strengths at different study sites (5). The use of contrast media, such as gadolinium, might further enhance spatial resolution, but concerns have been raised regarding the invasiveness of this approach and the ethics of using contrast, which may accumulate in brain tissue. Regardless of the type of magnet used, MRI is currently unable to detect rapid adjustments in blood flow and shear stress across physiologically relevant timespans. In contrast, Duplex ultrasound offers high temporal resolution, but is limited in terms of transcranial B mode imaging of arterial structure. In the current study we sought to combine the strengths of these distinct modalities and to apply computational biomechanics approaches to assess intracranial hemodynamics. Thus, we have introduced a valid, noninvasive, and safe platform to study the in vivo cerebrovascular structure-function interrelationship in humans.

However, there are also some limitations to our study. First, future studies could adopt our approaches to larger cohorts including dizygotic twins to fully elucidate the importance of genetics and environment on CoW structure and function. Second, due to the nature of the bifurcation in the posterior side

of the CoW, it is challenging to define comparable vessel segments, hence our exclusion of data in these regions. Third, we employed a rigid-wall CFD approach instead of compliant artery fluid-structure interaction (FSI) simulations; however, for accurate FSI, the material properties of the vessels are needed, and these data are currently unattainable in vivo. Fourth, the blood viscosity of each subject was unknown, and this could influence the hemodynamic metrics we report. It would be useful in future work to incorporate a viscosity model that accounts for this variation. Fifth, the downstream boundary conditions in the cerebral vascular bed (pressure or flow) cannot be accurately measured, and as such we developed an algorithm to estimate the percentage of blood flow to each region of the brain at these vessel outlets. The ability to measure in vivo conditions and advance the computational strategy used here would improve our data, but perhaps not negatively impact our findings.

In summary, our aims were to investigate the variance in the CoW geometry and understand its influence on CBF and vessel function under physiological conditions in healthy MZ twins. Using MRI and duplex Doppler ultrasound, we measured vessel hemodynamics, with further insight into the interrelationships of structure and function afforded using CFD modeling, to calculate shear stress and flow-derived metrics. We studied dynamic cerebrovascular responses to ecologically valid physiological conditions (hypercapnia and exercise). Despite similar physical characteristics and ~100% identical DNA between MZ twins, vessel diameter, length, tortuosity, and

bifurcation angle differed and resulted in even greater differences in functional measures; arteries behaved surprisingly differently between twin pairs in response to physiological stimuli. These data provide insight into structure-function relationships in a critical vascular territory in humans.

GRANTS

DISCLOSURES

No conflicts of interest, financial or otherwise, are declared by the authors.

AUTHOR CONTRIBUTIONS

H.J.T., C.E.M., K.J.S., D.J.G., and B.J.D. conceived and designed research; H.J.T., K.J.S., U.R., H.T.C., and D.J.G. performed experiments; H.J.T., U.R., H.T.C., L.J.K., K.J.S., D.J.G., and B.J.D. interpreted results of experiments; H.J.T., U.R., D.J.G., and B.J.D. drafted manuscript; H.J.T., H.T.C., L.J.K., K.J.S., D.J.G., and B.J.D. edited and revised manuscript; H.J.T., U.R., C.E.M., H.T.C., L.J.K., K.J.S., D.J.G., and B.J.D. approved final version of manuscript; U.R., H.T.C., L.J.K., and B.J.D. analyzed data; U.R., B.J.D., and H.T.C. prepared figures.

REFERENCES

1. **Berg P, Stucht D, Janiga G, Beuing O, Speck O, Thévenin D.** Cerebral blood flow in a healthy Circle of Willis and two intracranial aneurysms: computational fluid dynamics versus four-dimensional phase-contrast magnetic resonance imaging. *J Biomech Eng* 136: 041003, 2014. doi:10.1115/1.4026108.

2. **Celik IB, Ghia U, Roache PJ, Freitas CJ, Coleman H, Raad PE.** Procedure for estimation and reporting of uncertainty due to discretization in CFD applications. *J Fluids Eng* 130: 1–4, 2008. doi:10.1115/1.2960953.

3. **Chnafa C, Bouillot P, Brina O, Delattre BMA, Vargas MI, Lovblad KO, Pereira VM, Steinman DA.** Vessel calibre and flow splitting relationships at the internal carotid artery terminal bifurcation. *Physiol Meas* 38: 2044–2057, 2017. doi:10.1088/1361-6579/aa92bf.

4. **Doyle BJ, McGloughlin TM, Kavanagh EG, Hoskins PR.** *From Detection to Rupture: A Serial Computational Fluid Dynamics Case Study of a Rapidly Expanding, Patient-Specific, Ruptured Abdominal Aortic Aneurysm.* New York, NY: Springer, 2013, p. 53–68.

5. **Forgo B, Tarnoki AD, Tarnoki DL, Kovacs DT, Szalontai L, Persely A, Hernyes A, Szily M, Littvay L, Medda E, Szabo A, Kozak LR, Rudas G, Sas A, Sepsi M, Kostyal L, Olah C.** Are the variants of the circle of Willis determined by genetic or environmental factors? Results of a twin study and review of the literature. *Twin Res Hum Genet* 21: 384–393, 2018. doi:10.1017/thg.2018.50.

6. **Furchgott RF, Zawadzki JV.** The obligatory role of endothelial cells in the relaxation of arterial smooth muscle by acetylcholine. *Nature* 288: 373–376, 1980. doi:10.1038/288373a0.

7. **Green DJ, Hopman MT, Padilla J, Laughlin MH, Thijssen DH.** Vascular adaptation to exercise in humans: role of hemodynamic stimuli. *Physiol Rev* 97: 495–528, 2017. doi:10.1152/physrev.00014.2016.

8. **Green DJ, Jones H, Thijssen D, Cable NT, Atkinson G.** Flow-mediated dilation and cardiovascular event prediction: does nitric oxide matter? *Hypertension* 57: 363–369, 2011. doi:10.1161/HYPERTENSIONAHA.110.167015.

9. **Hoskins PR, Lawford PV, Doyle BJ.** *Cardiovascular Biomechanics.* New York, NY: Springer, 2017.

10. **John PS.** *Cerebral Blood Flow and Metabolism: A Quantitative Approach.* Singapore: World Scientific Publishing Company, 2017.

11. **Kim CS, Kiris C, Kwak D, David T.** Numerical simulation of local blood flow in the carotid and cerebral arteries under altered gravity. *J Biomech Eng* 128: 194–202, 2006. doi:10.1115/1.2165691.

12. **Lewis NC, Messinger L, Monteleone B, Ainslie PN.** Effect of acute hypoxia on regional cerebral blood flow: effect of sympathetic nerve activity. *J Appl Physiol (1985)* 116: 1189–1196, 2014. doi:10.1152/japplphysiol.00114.2014.

13. **Long Q, Luppi L, König CS, Rinaldo V, Das SK.** Study of the collateral capacity of the circle of Willis of patients with severe carotid artery stenosis by 3D computational modeling. *J Biomech* 41: 2735–2742, 2008. doi:10.1016/j.jbiomech.2008.06.006.

14. **Lynch AG.** *Towards the Development of Guidelines for the Surgical Treatment of Carotid Artery Disease: A Cranial Perfusion Approach.* Limerick, Ireland: Univ of Limerick, 2013.

15. **Massey BS, Ward-Smith J.** *Mech Fluid.* Boca Raton, FL: CRC, 1998.

16. **Moncada S, Palmer RM, Higgs EA.** Nitric oxide: physiology, pathophysiology, and pharmacology. *Pharmacol Rev* 43: 109–142, 1991.

17. **Moore S, David T.** A model of autoregulated blood flow in the cerebral vasculature. Proceedings of the Institution of Mechanical Engineers, Part H. *J Eng Med* 222: 513–530, 2008. doi:10.1243/09544119JEIM298.

18. **Moore S, David T, Chase JG, Arnold J, Fink J.** 3D models of blood flow in the cerebral vasculature. *J Biomech* 39: 1454–1463, 2006. doi:10.1016/j.jbiomech.2005.04.005.

19. **Moore SM.** *Computational 3D modelling of hemodynamics in the Circle of Willis.* Christchurch, New Zealand: Univ of Canterbury, 2007.

20. **Radaelli AG, Augsburger L, Cebral JR, Ohta M, Rüfenacht DA, Balossino R, Benndorf G, Hose DR, Marzo A, Metcalfe R, Mortier P, Mut F, Reymond P, Socci L, Verhegghe B, Frangi AF.** Reproducibility of haemodynamical simulations in a subject-specific stented aneurysm model–a report on the Virtual Intracranial Stenting Challenge 2007. *J Biomech* 41: 2069–2081, 2008. doi:10.1016/j.jbiomech.2008.04.035.

21. **Roache PJ.** Perspective: a method for uniform reporting of grid refinement studies. *J Fluids Eng* 116: 405–413, 1994. doi:10.1115/1.2910291.

22. **Thomas KN, Lewis NC, Hill BG, Ainslie PN.** Technical recommendations for the use of carotid duplex ultrasound for the assessment of extracranial blood flow. *Am J Physiol Regul Integr Comp Physiol* 309: R707–R720, 2015. doi:10.1152/ajpregu.00211.2015.

23. **Zarrinkoob L, Ambarki K, Wåhlin A, Birgander R, Eklund A, Malm J.** Blood flow distribution in cerebral arteries. *J Cereb Blood Flow Metab* 35: 648–654, 2015. doi:10.1038/jcbfm.2014.241.

24. **Zuleger DI, Poulikakos D, Valavanis A, Kollias SS.** Combining magnetic resonance measurements with numerical simulations–Extracting blood flow physiology information relevant to the investigation of intracranial aneurysms in the circle of Willis. *Int J Heat Fluid Flow* 31: 1032–1039, 2010. doi:10.1016/j.ijheatfluidflow.2010.07.003.